# SENSITIVITY IMPROVEMENT OF WIRELESS PRESSURE SENSOR BY INCORPORATING A SAW REFLECTIVE DELAY LINE

Haekwan Oh, Weng Wang, Keekeun Lee, Ikmo Park, and Sang Sik Yang*

Division of Electronics Engineering

Ajou University, Suwon, S. Korea, 443-749

*Email: ssyang@ajou.ac.kr

***Abstract - this paper presents a wireless surface acoustic wave (SAW) pressure sensor on 41°YX $LiNbO_3$ for tire pressure monitoring system (TPMS) application, in which a reflective delay line composed of an interdigital transducer (IDT) and several reflectors was used as the sensor element. Using the coupling of modes (COM), the SAW reflective delay line was simulated, and the optimal design parameters were determined. The fabricated 2.4GHz SAW sensor was wirelessly characterized by the network analyzer. Sharp reflection peaks, few spurious signals, and relatively high signal-to-noise (S/N) ratio were observed. High sensitivity of 2.9 deg/kPa and good linearity were observed.***

**Index terms: coupling of modes, interdigital transducer, $LiNbO_3$, piezoelectric substrate, reflective delay line, surface acoustic wave, wireless pressure sensor, temperature compensation**

## I. INTRODUCTION

Recently, surface acoustic wave (SAW) pressure sensors have gained an increasing amount of attention for wireless tire pressure monitoring systems (TPMSs), owing to their high sensitivity, small size, low cost, easy reproducibility, and good stability [1-2]. Typical SAW based pressure sensors are composed of two resonators. One is placed in the sensing area (in the center of the diaphragm) and the other is used as a reference sensor to compensate the temperature effect (depending on its location on the substrate). A differential frequency output

signal is used to evaluate the pressure information. Many research groups have successfully presented SAW pressure sensors with different designs and structures [1-2]. However, due to the high temperature sensitivity of the resonance frequency of the surface acoustic wave resonator (SAWR), the output signal of the sensor system is degraded by the influence of the resonant parts of the radio channel, antennas and matching networks. Moreover, even when differential structures such as dual SAWRs are used for the sensor system, the temperature effect cannot be effectively compensated, because the temperature is not measured at the same location as the pressure sensor [3].

To overcome the disadvantages of the current SAW pressure sensor, a reflective delay line patterned with an interdigital transducer (IDT) and several reflectors on a piezoelectric substrate was presented as the pressure sensor element [4-6]. This device shows some unique advantages over other currently available devices: (1) it is small, light and has a simple measurement system, owing to its one-chip architecture; (2) it is possible to compensate temperature effect; and (3) during the sensitivity evaluation, phase shifts provide it with a much higher resolution. However, this type of device still has the following drawbacks: (i) no systematic theoretical simulation for the device performance improvement, (ii) high propagation loss, (iii) a high level of spurious signals, and (iv) a relatively low signal-to-noise (S/N) ratio. Therefore, in this paper, we describe an optimal design for a SAW pressure sensor which is accomplished by the coupling of modes (COM) and theoretical analysis of the sensor response mechanism, in order to determine the optimal design parameters.

For TPMS applications, we fabricated 2.4GHz SAW-based wireless pressure sensors. A $41^{o}$ YX $LiNbO_3$ piezoelectric substrate was used, which provide a leaky shear horizontal (SH) SAW mode with high SAW propagation velocity (4792.2m/s) and large electromechanical coupling factor $K^2$ (17.2%) [7]. Figure 1 shows a schematic diagram of the SAW pressure sensors. An RF pulse is transmitted from the network analyzer to a SAW transponder through the antennas. The interdigital transducer (IDT) converts the electromagnetic (EM) signals into mechanical acoustic waves. The SAW propagates on the piezoelectric substrate and is partially reflected by the reflectors. The reflected waves are reconverted into an EM wave by the IDT and are transmitted back to the network analyzer. A mechanical force induces the bending of the diaphragm. The bending changes the SAW propagation length and velocity,

resulting in the phase shifts of the reflected peaks depending on the applied pressure value. By evaluating the phase shifts, we can extract the external pressure values.

To find the optimal design parameters, the coupling of modes (COM) modeling and finite element methods (FEMs) were performed. The device was fabricated according to the extracted design parameters and then wirelessly characterized using an RF network analyzer. In this paper, we describe the process used to create reliable SAW sensor structures, their electrical and mechanical performance, and a comparison between the simulated and measured results.

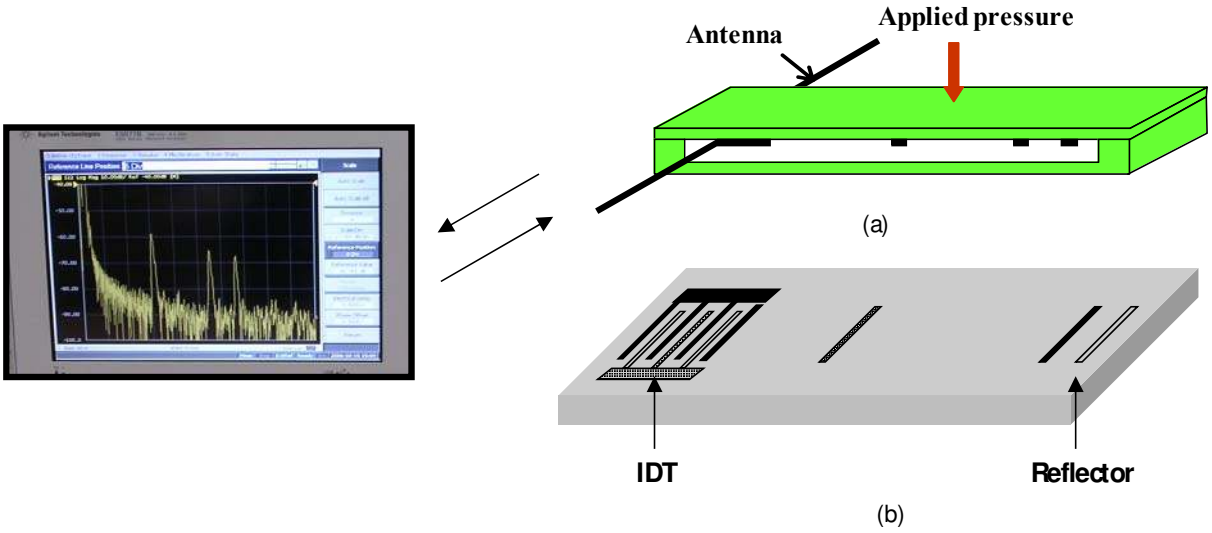


Figure 1. Schematic diagram of the SAW pressure sensor system. (a) 3-dimensional view of the SAW pressure sensor and (b) flip-over view of the top diaphragm.

## II. THEORETICAL ANALYSIS OF SENSOR RESPONSE MECHANISM

A mechanical analysis of SAW propagation on the pre-stressed piezoelectric diaphragm was studied using FEM stress analysis [8]. The basic structure of the pressure sensor and coordinate system are shown in Figure 2. The sensor is composed of a piezoelectric diaphragm (example of 41° YX $LiNbO_3$) and a sensor cover. The SAW propagates along the $x_1$ axis on the $x_1$-$x_2$ plane at $x_3$=0. For the analysis, all of the material parameters of the medium are transformed into this coordinate system. Using the wave motion equations and electrical boundary conditions at $x_3$=0, a set of equations for the stress $T$ *and* electric displacement $D$, the SAW displacement $U$ and the electrical potential $\varphi$ are given by Eq. (1).

$$\begin{cases} T_{ij} = C_{ijkl}\partial U_k / \partial x_l + e_{kij}\partial\varphi / \partial x_k, D_i = e_{ikl}\partial U_k / \partial x_l - \varepsilon_{ik}\partial\varphi / \partial x_k \\ C_{ijkl}\partial^2 U_k / \partial x_i \partial x_l + e_{kij}\partial^2\varphi / \partial x_k \partial x_i = \rho \times \partial^2 U_j / \partial^2 t \\ e_{ikl}\partial^2 U_k / \partial x_l \partial x_i - \varepsilon_{ik}\partial^2\varphi / \partial x_k \partial x_i = 0 \end{cases}, \quad (1)$$

where $\rho$ is the density and $C_{ijkl}$, $e_{ikl}$, $\varepsilon_{ik}$ ($i,j,k,l$ = 1,2,3) are the stiffnesses, piezoelectric coefficients and components of permittivity of the $LiNbO_3$, respectively. Einstein's summation rule was used, and the indices can be varied from 1 to 3.

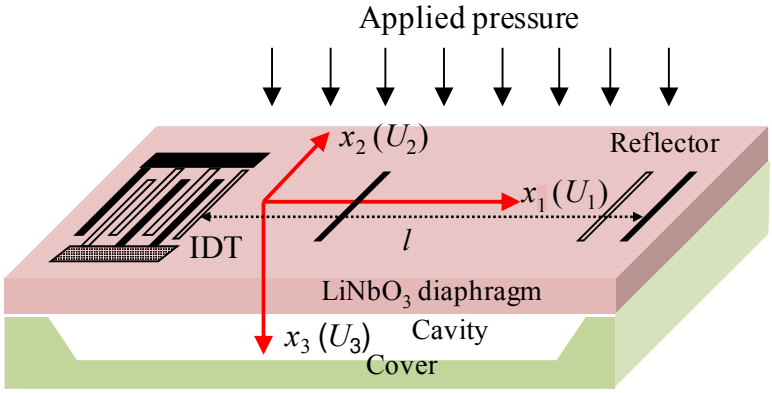


Figure 2. Basic structure of SAW pressure sensor and coordinate system for SAW propagation analysis.

Considering a shear horizontal (SH) type leaky SAW propagating on a 41° YX $LiNbO_3$ substrate (Euler angles: (0°, -49°, 0°)), $U_1$ and $U_3$ are 0 [7]. The displacement $U_2$ and the potential $\varphi$ decrease as $x_3$ increases and vanish at infinity. Therefore, the solutions of Eq. (1) have the following forms:

$$\begin{cases} U_2 = \beta_1 \exp(-\alpha k x_3) \times \exp(i\omega t - ikx_1) \\ \varphi = \beta_2 \exp(-\alpha k x_3) \times \exp(i\omega t - ikx_1) \end{cases}, \quad (2)$$

where $\beta_1$ and $\beta_2$ are the normalized amplitudes, $k = \omega/v = 2\pi/\lambda$ is the wave number, $\alpha$ is a decay constant, and $v$ is the phase velocity of the SAW. In order to ensure the decay of the displacement $U_2$ and the potential $\varphi$ along $x_3$, generally the complex constant $\alpha$ must have a negative imaginary part. Substituting Eq. (2) into Eq. (1), a set of linear homogeneous equations for the normalized amplitudes $\beta_1$ and $\beta_2$ is obtained,

$$\begin{bmatrix} C_{66} + C_{44}a^2 - \rho v^2 & e_{16} + e_{34}a^2 \\ -(e_{16} + e_{34}a^2) & \varepsilon_{11} + \varepsilon_{33}a^2 \end{bmatrix} \begin{bmatrix} \beta_1 \\ \beta_2 \end{bmatrix} = 0. \quad (3)$$

This set of equations has a nontrivial solution if the determinant of the coefficients is the

following,

$$\begin{bmatrix} C_{66}+C_{44}a^2-\rho v^2 & e_{16}+e_{34}a^2 \\ -(e_{16}+e_{34}a^2) & \varepsilon_{11}+\varepsilon_{33}a^2 \end{bmatrix} = 0. \qquad (4)$$

Eq. (4) is an algebraic equation of the fourth order in $\alpha$ so that for a given value of the SAW velocity $v$ we obtain two eigenvalues of $\alpha$ with a negative imaginary part. For both eigenvalues of $\alpha$, the eigenvectors $\beta_1$ and $\beta_2$ of the normalized amplitudes of Eq. (1) vanish at infinity from Eq. (3). Then $U_2$ and $\varphi$ are represented as

$$\begin{cases} U_2 = \sum_{n=1}^{2} A_n \beta_{1n} \exp(-\alpha_n k x_3) \times \exp(i\omega t - ikx_1) \\ \varphi = \sum_{n=1}^{2} A_n \beta_{2n} \exp(-\alpha_n k x_3) \times \exp(i\omega t - ikx_1) \end{cases}, \qquad (5)$$

with $A_n$ as the normalized amplitudes.

For the full description of the SAW, the electric potential $\varphi$, the electric displacement along the $x_3$ direction $D_3$ and the stress $T_{3i}$ ($i$=1,2) must satisfy the boundary continuity conditions at $x_3$=0. The mechanical stress continuity conditions are described by Eq. (6).

$$\begin{aligned} T_{31}|_{x_3=0} &= T_x \\ T_{32}|_{x_3=0} &= T_y \end{aligned}, \qquad (6)$$

where $T_x$ and $T_y$ are the applied stress components which are calculated by FEM analysis. The electric displacement continuity boundary conditions are described by Eq. (7).

$$\begin{cases} D_3 = e_{3kl}\partial U_k/\partial x_l - \varepsilon_{ik}\partial\varphi/\partial x_k \text{ (for } x_3>0) \\ D_{30} = -\varepsilon_0 \partial\varphi'/\partial x_3 \text{ (for } x_3<0),\ \varphi' = \varphi|_{x_3=0} \times \exp(kx_3) \\ D_3|_{x_3=0} = D_{30}|_{x_3=0} \end{cases} \qquad (7)$$

where $\varepsilon_0$ is the vacuum dielectric constant. The substitution of the general solution, Eq. (5), into the boundary conditions leads to a second set of homogeneous linear equations forming the normalized amplitudes $\beta_1$ and $\beta_2$. A nontrivial solution again requires that the determination vanishes at an assumed velocity value, i.e.,

$$\begin{bmatrix} c_{56}+e_{15}k_1-c_{44}\lambda a_1-e_{34}\lambda k_1 a_1 & c_{56}+e_{15}k_2-c_{44}\lambda a_2-e_{34}\lambda k_2 a_2 \\ e_{34}a_1-\varepsilon_{31}k_1-\varepsilon_{33}k_1 a_1-j\varepsilon_0 k_1 & e_{34}a_2-\varepsilon_{31}k_2-\varepsilon_{33}k2a_2-j\varepsilon 0k_2 \end{bmatrix}=0 \quad (8)$$

$$k_1=(e_{16}+e_{34}a_1{}^2)/(\varepsilon_{11}+\varepsilon_{33}a_1{}^2)$$

$$k_2=(e_{16}+e_{34}a_2{}^2)/(\varepsilon_{11}+\varepsilon_{33}a_2{}^2)$$

$$\lambda=T_x/T_y$$

Then, using the iterative method, for a given stress distribution along the diaphragm, the SAW velocity change $\Delta v/v$ depending on the applied pressure can be calculated from the derivation using above equations. The relative phase change $\Delta\Phi/\Phi$ along the diaphragm can also be determined from the velocity change $\Delta v/v$ and $\Delta l/l$ which is the SAW propagation distance mentioned in Fig. 2 by Eq. (9)

$$\Delta\Phi/\Phi=\Delta l/l-\Delta v/v. \quad (9)$$

To determine the diaphragm bending and stress distribution along the diaphragm of the pressure sensor, the finite element method (FEM) was used. Figure 3 shows the calculated stress distribution on the diaphragm surface along the SAW propagation direction on the 41° YX $LiNbO_3$ substrates with sizes of 20mm×8mm×350μm and 20mm×8mm×500μm in the case of a pressure of 300kPa. The different stress distributions resulting from the various diaphragm thicknesses result in different relative phase changes along the diaphragm. Figure 4 shows the calculated relative phase change along the $LiNbO_3$ diaphragms with different thicknesses. Better sensitivity was observed from 350μm $LiNbO_3$ than from 500μm Y-cut quartz [6]. The picture in Figure 3 shows that: (1) the proper thickness of the $LiNbO_3$ diaphragm makes it possible to obtain better sensitivity than quartz, (2) there is a sign change of the relative phase change over the diaphragm area. Using the method of difference (MOD) and proper positioning of the SAW reflectors (example of a reflective delay line with three reflectors), as shown in Figure 4, it is possible to compensate the temperature effect and obtain a higher absolute value for the sensor information according to the equation:

$$\Delta\Phi=\Delta\Phi_{2\text{-}1}-w\times\Delta\Phi_{3\text{-}2}=(\Phi_2-\Phi_1)-w\times(\Phi_3-\Phi_2), \quad (10)$$

where the weighting factor $w=l_1/l_2$, and $l_1$ and $l_2$ are the distances between the reflectors, which were determined by the FEM analysis [6]. Usually, the first and second reflectors are placed in the stretched and compressed areas, respectively; the latter one is placed at the end of the compressed section. The acoustic wave velocity is slower in the stretched section,

whereas it is faster in the compressed section. $\Phi_i$ ($i$=1,2,3) are the relative phase changes of the $i^{th}$ reflector ($R_1$, $R_2$ and $R_3$ in Figure 4).

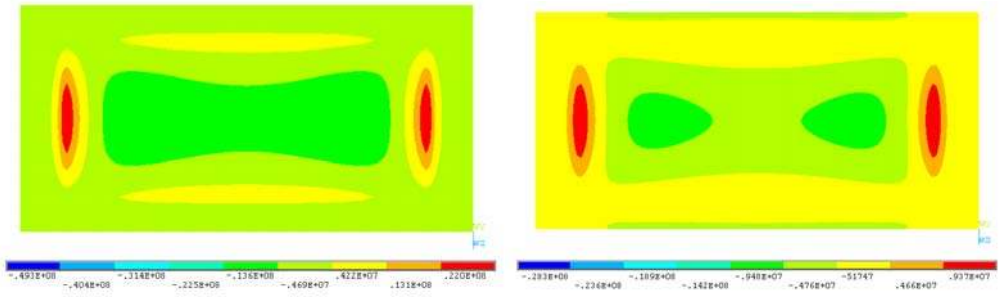

Figure 3. Calculated stress distribution on $LiNbO_3$ diaphragm under 300kPa pressure in cases of (a) 350μm thick diaphragm and (b) 500μm thick diaphragm.

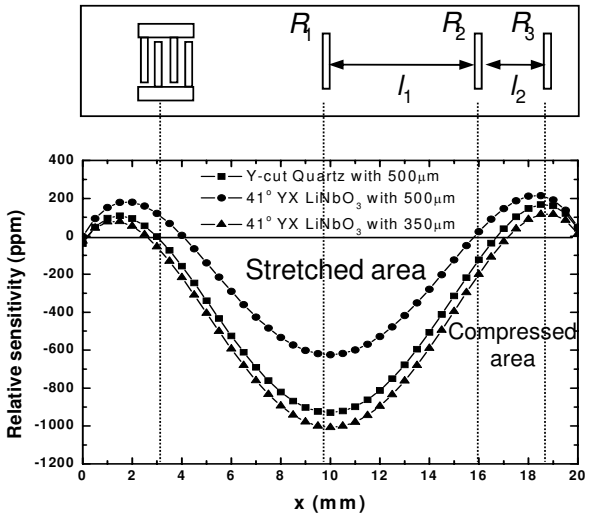


Figure 4. Relative phase changes along the SAW propagation path in case of Y cut quartz and 41° YX $LiNbO_3$ under 300kPa pressure.

Also, Figure 4 shows that varying the diaphragm thickness results in the variation of the diaphragm bending, strain/stress distribution, and corresponding velocity change. The effect of the piezoelectric diaphragm thickness on the sensitivity of the sensor (calculated from Eq. (10)) was evaluated and shown in Figure 5, in which the simulation parameters are as follows: 41° YX $LiNbO_3$ substrate, operation frequency substrate of 2.4GHz and diaphragm area of 8 mm×4 mm. The thickness was varied from 150μm to 400μm. Figure 5 shows the calculated phase shift of the sensor with respect to the diaphragm thickness under a pressure of 200kPa.

It shows that the sensitivity increases as the diaphragm thickness decreases, due to the marked bending under the applied pressure. However, a very thin thickness will decrease the endurance of the diaphragm, thus resulting in a small pressure sensing range.

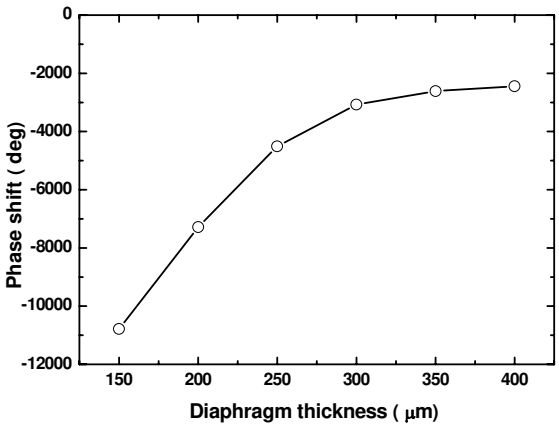


Figure 5. Calculated phase shift as function of diaphragm thickness at pressure of 200kPa.

## III. COUPLING OF MODE (COM) MODELING OF SAW DEVICE

COM modeling is a very efficient technique for the analysis of SAW devices [9]. We previously reported the simulation of SAW reflective delay lines with various IDT structures and reflector configurations using COM modeling [10]. The two and three dimensional mixed matrix (*P*-matrix) representations are used to present the solutions of the COM equations for the IDT and reflectors and referred to as $P_{IDT}$ and $P_{Ref}$, respectively. By solving the *P*-matrix elements, the two-dimensional admittance matrix, Y, can be expressed as

$$Y = \begin{bmatrix} y_{11} & y_{12} \\ y_{21} & y_{22} \end{bmatrix}. \qquad (11)$$

where

$$y_{11} = P_{IDT33} + \frac{P_{Ref11} P_{IDT32} P_{IDT23}}{1 - P_{Ref11} P_{IDT22}}, \quad y_{12} = \frac{P_{Ref13} P_{IDT32}}{1 - P_{Ref11} P_{IDT22}}, \quad y_{21} = \frac{P_{Ref31} P_{IDT23}}{1 - P_{Ref11} P_{IDT22}}, \quad y_{22} = P_{Ref33} + \frac{P_{IDT22} P_{Ref13} P_{Ref31}}{1 - P_{Ref11} P_{IDT22}}$$

Using the admittance matrix solution, the reflection coefficient $S_{11}$ can be deduced by

$$S_{11} = \frac{(Y_G - y_{11}) \times (Y_G + y_{22}) + y_{12} \times y_{21}}{(Y_G + y_{11}) \times (Y_G + y_{22}) - y_{12} \times y_{21}} \qquad (12)$$

where $Y_G$ is the resource and load inductance. $S_{11}$ in the frequency domain can be transformed into the time domain through the FFT program.

440MHz SAW reflective delay lines with three types of reflectors and different IDT structures (bidirectional IDTs and SPUDT structures) were simulated. The SH wave on a 41° YX $LiNbO_3$ piezoelectric substrate has a high SAW propagation velocity and large $K^2$. A high SAW velocity provides easy device patterning in the fabrication process. A large value of $K^2$ allows for high reflectivity from the reflectors and a low insertion loss. Figure 6 shows the simulated reflection coefficient $S_{11}$ in the frequency and time domains in the case of 41° $LiNbO_3$, an operation frequency of 2.4GHz, aluminum IDT with 10 finger pairs, 50λ aperture size, and three shorted grating reflectors. The other parameters used in the COM simulation were obtained from Ref. 9. From the simulated results, sharp reflection peaks, a high S/N, and low spurious noise between the reflection peaks were observed. Also, a SAW reflective delay line with a shorted grating reflector, smaller number of IDT finger pairs (10~20), and smaller acoustic aperture in the simulated results would be expected to show better performance.

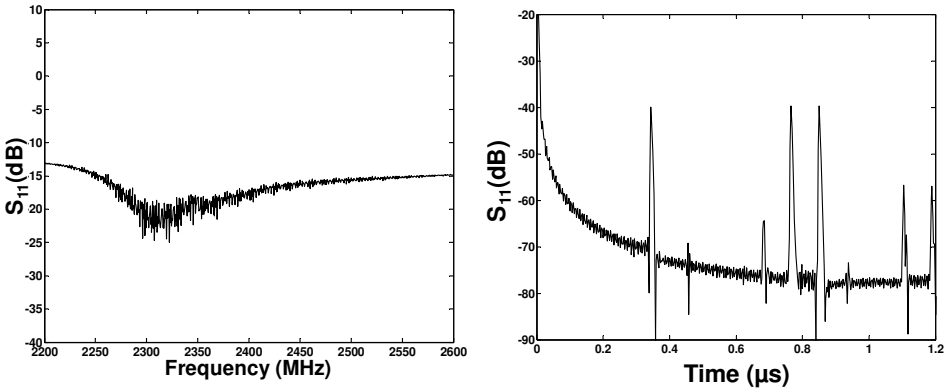


(a) (b)

Figure 6. Simulated $S_{11}$ (a) in frequency domain and (b) in time domain

## IV. FABRICATION OF THE SAW SENSOR

The primary goals of the SAW pressure sensors are sharp reflection peaks with a small attenuation, a long readout distance at 2.4GHz, and high pressure sensitivity. Relatively thin 41° YX $LiNbO_3$ was used as the piezoelectric substrate, because it has a high SAW propagation velocity, large electromechanical coupling factor, and leaky SAW propagation mode. A high $K^2$ enables greater reflection from the reflectors, in conjunction with a lower

insertion loss. Leaky-SAW devices are less sensitive to surface contamination and have a high RF power handling capability. A thin diaphragm thickness provides better sensitivity than a thicker one, so a 350μm $LiNbO_3$ diaphragm was used. A uniform IDT structure was designed. The IDT width was ~0.45μm. The distance between the IDT and the first reflector was set to 624μm to separate the reflected peaks from the initial environmental noise peaks.

The fabrication procedure of the pressure sensor is shown in Figure 7. A 100nm thick aluminum layer was deposited on the 41° YX $LiNbO_3$ piezoelectric substrate (Figure 7(a)). MA-2403 electron beam resist was spin-coated and patterned by electron beam lithography (EBL) (Figure 7(b)). The exposed resist was developed and then reactive ion etching was used to etch the aluminum (Figure 7(c)). The resist was removed by acetone (Figure 7(d)). Next, a 250μm deep cavity on the heavily doped silicon substrate was made in TMAH solution (Figure 7(e-f)). The heavily doped silicon substrate provides low resistivity like a metal. Gold was deposited over the cavity using sputtering for ground shielding (Figure 7(g)). The $LiNbO_3$ diaphragm was then attached to the silicon substrate with an epoxy (Figure 7(h)). A 2-dimensional planar antenna with a central frequency of 2.39GHz and bandwidth of 21 MHz was fabricated using an 8 mil-thick RO4003 substrate (dielectric constant *k*: ~3.38) and then wire-soldered to complete the electrical connection.

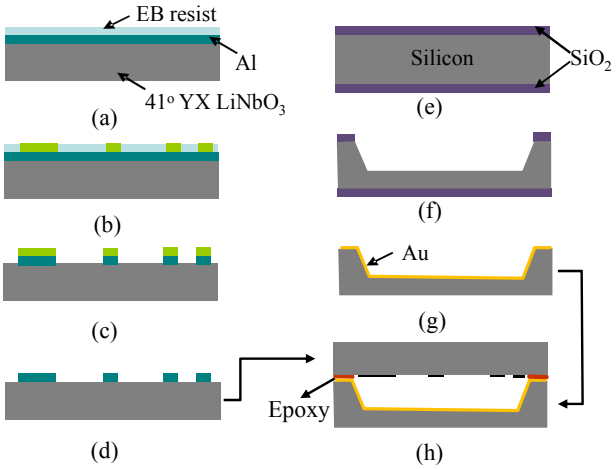


Figure 7. The fabrication procedure: (a) Al deposition and spin coating of electron beam (EB) resist, (b) EB exposure, (c) IDT and reflectors patterns by reactive ion etch (RIE), (d) EB resist removal, (e) $SiO_2$ growth, (f) $SiO_2$ and Si wet-etching in TMAH, (g) $SiO_2$ removal and ground shielding with gold, and (h) wafer bonding with epoxy.

## V. RESULTS AND DISCUSSION

a. Fabricated SAW devices

The fabricated device was visualized by optical microscopy and scanning electron microscopy (SEM), as shown in Figures 8(a-b). There were 10 IDT finger pairs with a width of ~0.45μm and overlapping aperture of 91μm (50λ). Three bar-type reflectors were placed along the SAW propagation direction. The distance between the IDT and the first reflector was 624μm, and the ratio of the distance between the first and second reflectors to that between the second and third reflectors was 3. The piezoelectric substrate was attached to the bottom silicon substrate with a 250μm deep cavity using an epoxy adhesive, as shown in Figure 8(b). The sizes of the signal and ground pads on the device were well matched with the coaxial cable used for the RF measurement.

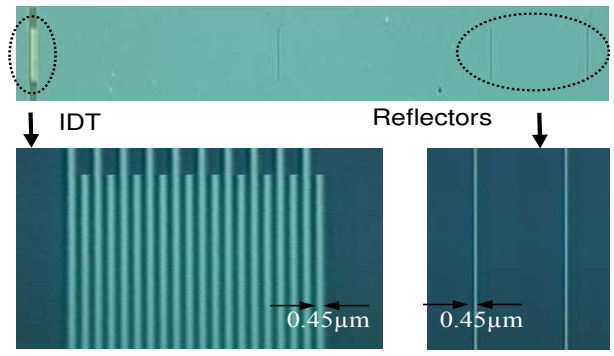


(a)

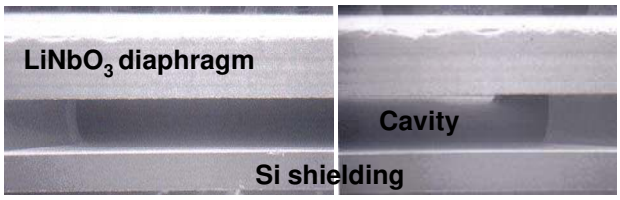


(b)

Figure 8. (a) Optical view of top diaphragm and magnified IDT and reflectors. (b) Cross-sectional view of the completed device.

b. Wireless electrical measurement

The reflection coefficient $S_{11}$ was measured wirelessly using HP 8510 network analyzer, as shown in Figure 9(a). The frequency was swept from 2.25GHz to 2.45GHz with an RF power of 10dBm. Three sharp peaks were observed from all three reflectors. The *x*-axis represents

the travel time of the impulse and the *y*-axis represents the averaged reflection over the frequency range. The first reflection occurred at 0.26μs, and the second and third ones at 0.55μs and 0.65μs, respectively. All of the reflected peaks were well matched with the predicted values obtained from the simulation (Figure 9(b)). Based on these promising results, we concluded that (1) all of the device parameters had good impedance matching with the propagating SAW, due to very precise device patterning obtained using the EBL, (2) the newly employed ground shielding worked very well, which reduced the coupling loss of the propagating SAW energy to the surrounding atmosphere and protected the fabricated SAW device from random variations such as noise and other environment factors during network analyzer testing, and (3) the use of a high $K^2$ substrate provided a large reflection from the reflectors and small insertion loss.

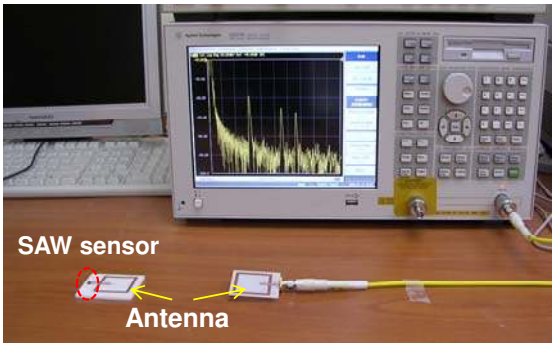


(a)

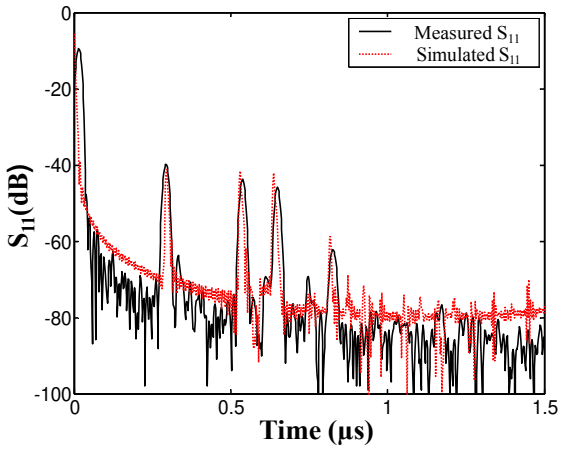


(b)

Figure 9. (a) The wireless $S_{11}$ measurement of the fabricated SAW device using HP network analyzer and (b) comparison between the measured $S_{11}$ and simulated one

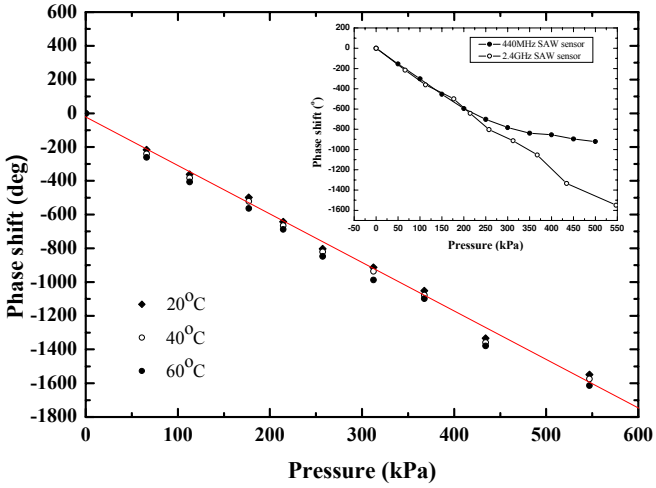


Figure 10. Sensitivity evaluation of the fabricated 2.4GHz SAW pressure sensor. (Inset: sensitivity comparison between 440MHz and 2.4GHz SAW pressure sensors)

c. Sensitivity evaluation

A mechanical compression force was applied to the diaphragm by placing an object at its center, and then the $S_{11}$ parameter was measured by the Network analyzer, and the time deviation of the reflected peaks, $\Delta\tau$, as function of the amount of applied mechanical force was extracted using a parabolic approximation [11]. The phase shifts of the reflected peaks $\Phi_i$ were obtained from the relation: $\Phi_i = 2\pi f \times \Delta\tau$ ($i$=1,2,3). Then, using Eq. 10, the pressure sensing information was determined. Figure 10 shows the measured phase shifts versus the applied mechanical pressure at testing temperatures of 20°C, 40°C and 60°C. High linearity was observed up to 500kPa. The nonlinearity was 2.5%FS. The pressure sensitivity was evaluated as 2.9 deg/kPa.

A sensitivity comparison with the 440MHz SAW pressure sensor mentioned in Ref. [12] was performed, as shown in the inset of Figure 10. Similar pressure sensitivities were observed for the two sensors. In general, it is known that a higher frequency device has better sensitivity than a lower frequency one, but that the sensitivity also depends on the geometry of the device, such as its diaphragm size and thickness. The 440MHz pressure sensor has a large device size, whereas the 2.4GHz device has a very small diaphragm area. Another observation is that in the 2.4GHz device, a higher linearity range was obtained than in the 440MHz SAW sensor, because of the smaller size of the diaphragm. The temperature dependence effect of the fabricated sensor was tested on a hotplate. Temperature insensitivity was observed in the

temperature range from 20 to 60$^{o}$C (Figure 10). No noticeable deviation of the phase shifts was observed, because the temperature effect was compensated by the DOM [6]. Based on these results, we suggest that this prototype SAW pressure sensor is very promising for achieving wirelessly requestable and batteryless TPMS applications.

## VI. CONCLUSION

This paper presents a wireless SAW pressure sensor incorporating a 2.4GHz reflective delay line for TPMS applications. A theoretical modeling was performed to predict the SAW propagation behavior along the pre-stressed piezoelectric substrate. The effects of the diaphragm type and geometrical characteristics on the sensor performance were investigated. The fabricated 2.4GHz SAW device was wirelessly characterized by an HP network analyzer. Sharp reflection peaks, a high S/N ratio, low wave attenuation, and low spurious noise between the reflection peaks were observed. The measured $S_{11}$ agrees well with the simulated result. The pressure sensing experiments showed satisfactory results such as a high sensitivity of 2.9 deg/kPa and good linearity up to 500 kPa.

## REFERENCES

[1] W. buff, S. Klett and M. Rusko, “Passive remote sensing for temperature and pressure using SAW resonator devices,” IEEE Transaction on UFFC, Vol. 45, No. 5, 1998, pp. 1388-1392.

[2] R. Lohr and P. Vickery, “SAW based TPMS: the next revolution for tires,” Tire Technology EXPO 2005, Cologne, Germany, Feb. 22-24, 2005.

[3] C. Muller, T. Nirmaier and A. Rugemer, “Sensitive $NO_2$ detection with surface acoustic wave devices using a cyclic measuring technique,” Sensors and Actuators B, Vol. 68, 2000, pp. 69-73.

[4] G. Scholl, F. Schmidt and U. Wolff, “Surface Acoustic Wave Devices for Sensor Applications,” Phys. Stat. Sol., Vol. 185, No. 1, 2001, pp.47–58.

[5] H. Sched, G. Scholl, F. Seifert and R. Weige1, “Quartz pressure sensor based on SAW reflective delay line,” Proceeding of IEEE Ultrasonics Symp., 1996, pp. 347-350.

[6] M. Jungwirth, H. Scherr and R. Weigel, “Micromechanical precision pressure sensor

incorporating SAW delay lines," Acta Mechanica, Vol. 158, 2002, pp. 227-252.

[7] H. Kenya, Surface Acoustic Wave Devices in Telecommunications – Modeling and Simulation Springer Verlag, 2000.

[8] D. P. Mogen, "Surface wave devices for signal processing," NewYork: Elseview, 1985.

[9] V. Plessky and J. Koskela, "Coupling-of-modes analysis of SAW devices," International Journal of High Speed Electronics and Systems, Vol. 10, 2000, pp. 867-947.

[10] W. Wang, K. Lee, I. Woo, I. Park and S. Yang, "Optimal design on SAW sensor for wireless pressure measurement based on reflective delay line," Sensors and Actuators A, Vol. 139, 2007, pp. 2-6.

[11] L. M. Reindl and I. M. Shrena, "Wireless measurement of temperature using surface acoustic waves sensors," IEEE transctions on Ultrsonics, Ferroelectrics, and Frequency control, Vol. 51, No. 11, 2004, pp. 1457-1463.

[12] K. Lee, W. Wang, T. Kim and S.Yang, "A novel 440MHz wireless SAW microsensor integrated with pressure-temperature sensors and ID tag," J. Micromech. Microeng., Vol. 17, 2007, pp. 515-523.